

The Ionized Gas and Nuclear Environment in NGC 3783

II. Averaged *HST*/STIS and *FUSE* Spectra¹

Jack R. Gabel², D. Michael Crenshaw³, Steven B. Kraemer⁴, W. N. Brandt⁵, Ian M. George^{6,7}, Frederick W. Hamann⁸, Mary Elizabeth Kaiser⁹, Shai Kaspi^{5,10}, Gerard A. Kriss^{9,11}, Smita Mathur¹², Richard F. Mushotzky⁶, Kirpal Nandra^{6,13}, Hagai Netzer¹⁰, Bradley M. Peterson¹², Joseph C. Shields¹⁴, T. J. Turner^{6,7}, & Wei Zheng⁹

ABSTRACT

We present observations of the intrinsic absorption in the Seyfert 1 galaxy NGC 3783 obtained with the Space Telescope Imaging Spectrograph (STIS) on the *Hubble Space Telescope* (*HST*) and the *Far Ultraviolet Spectroscopic Explorer* (*FUSE*). We have combined 18 STIS and 5 *FUSE* observations to obtain a high signal-to-noise averaged spectrum spanning 905–1730 Å. The averaged spectrum reveals absorption in O VI, N V, C IV, N III, C III and the Lyman lines up to Ly ϵ in the three blueshifted kinematic components previously detected in the STIS spectrum (at radial velocities of -1320 , -724 , and -548 km s⁻¹). The highest velocity component exhibits absorption in Si IV. We also detect metastable C III in this component, indicating a high density in this absorber. No lower ionization lines, i.e., C II and Si II, are detected. A weak, fourth absorption component is tentatively detected in the high ionization lines and Ly α and Ly β at a radial velocity of -1027 km s⁻¹. The Lyman lines reveal a complex absorption geometry. The strength of the higher order lines indicates Ly α and Ly β are saturated over much of the resolved

¹Based on observations made with the NASA/ESA *Hubble Space Telescope*. STScI is operated by the Association of Universities for Research in Astronomy, Inc. under NASA contract NAS 5-26555.

²The Catholic University of America/IACS, NASA/Goddard Space Flight Center, Laboratory for Astronomy and Solar Physics, Code 681, Greenbelt, MD 20771.

³Department of Physics and Astronomy, Georgia State University, Atlanta, GA 30303.

⁴The Catholic University of America, NASA/Goddard Space Flight Center, Laboratory for Astronomy and Solar Physics, Code 681, Greenbelt, MD 20771.

⁵Department of Astronomy and Astrophysics, 525 Davey Laboratory, The Pennsylvania State University, University Park, PA 16802.

⁶Laboratory for High Energy Astrophysics, NASA/Goddard Space Flight Center, Code 662, Greenbelt, MD 20771.

⁷Joint Center for Astrophysics, Physics Department, University of Maryland, Baltimore County, 1000 Hilltop Circle, Baltimore, MD 21250.

⁸Department of Astronomy, University of Florida, 211 Bryant Space Science Center, Gainesville, FL, 32611-2055.

⁹Center for Astrophysical Sciences, Department of Physics and Astronomy, The Johns Hopkins University, Baltimore, MD 21218-2686.

¹⁰School of Physics and Astronomy, Raymond and Beverly Sackler Faculty of Exact Sciences, Tel-Aviv University, Tel-Aviv 69978, Israel.

¹¹Space Telescope Science Institute, 3700 San Martin Drive, Baltimore, MD 21218.

¹²Department of Astronomy, Ohio State University, 140 West 18th Avenue, Columbus, OH 43210-1173.

¹³Universities Space Research Association, 7501 Forbes Boulevard, Suite 206, Seabrook, MD 20706-2253.

¹⁴Department of Physics and Astronomy, Clippinger Research Labs 251B, Ohio University, Athens, OH 45701-2979.

profiles in the three strongest absorption components and, therefore, their observed profiles are determined by the covering factor. We separate the individual covering factors of the continuum and emission-line sources as a function of velocity in each kinematic component using the Ly α and Ly β lines. The covering factor of the BLR is found to vary dramatically between the cores of the individual kinematic components, ranging from 0 to 0.84. Additionally, we find that the continuum covering factor varies with velocity within the individual kinematic components, decreasing smoothly in the wings of the absorption by at least 60%. Comparison of the effective covering factors derived from the H I results with those determined directly from the doublets reveals the covering factor of Si IV is less than half that of H I and N V in the high velocity component. Additionally, the FWHM of N III and Si IV are narrower than the higher ionization lines in this component. These results indicate there is substructure within this absorber. We also find evidence for structure in the column density profiles of the high ionization lines in this component. We derive a lower limit on the total column ($N_H \geq 10^{19} \text{ cm}^{-2}$) and ionization parameter ($U \geq 0.005$) in the low ionization subcomponent of this absorber. The metastable-to-total C III column density ratio implies $n_e \approx 10^9 \text{ cm}^{-3}$ and an upper limit on the distance of the absorber from the ionizing continuum of $R \leq 8 \times 10^{17} \text{ cm}$. The decreasing covering factor found in the wings of the absorption and the extreme compactness of the C III* absorber are suggestive of a clumpy absorption gas with low volume filling factor.

Subject headings: galaxies: individual (NGC 3783) — galaxies: active — galaxies: Seyfert — ultraviolet: galaxies

1. Introduction

Observations with the *Hubble Space Telescope* (*HST*) have revealed that intrinsic UV absorption is a common phenomenon in Seyfert 1 galaxies, appearing in over half of the objects with available spectra (Crenshaw et al. 1999). The UV absorption resonance lines are typically blueshifted in the rest frames of the host galaxies, indicating radial outflow. The absorption is often highly variable and, in some cases, only partially covers the continuum and emission-line regions of the active nuclei, which implies the absorbers are intrinsic to the AGN environments. The observed variations may be due to changes in ionization in the absorbers (Krolik & Kriss 1997; Shields & Hamann 1997; Crenshaw et al. 2000) or changes in the total absorbing column, i.e., as a result of motion into and out of our line-of-sight (Crenshaw & Kraemer 1999).

NGC 3783 is a bright Seyfert 1 galaxy that exhibits strong UV absorption features and X-ray “warm absorption”. Several observations with *HST* over the past decade have revealed dramatic variability in the UV absorption. NGC 3783 also has a highly variable UV continuum source. An *International Ultraviolet Explorer* (*IUE*) monitoring campaign revealed a factor of ~ 2 flux variations over timescales of 20–40 days (Reichert et al. 1994; Onken & Peterson 2002).

Intrinsic absorption in Ly α and C IV $\lambda\lambda 1548, 1551$ was first detected in NGC 3783 with Faint Object Spectrograph (FOS) observations by Reichert et al. (1994). Three subsequent spectra obtained over a period of about two years with the Goddard High Resolution Spectrograph (GHRS) revealed highly variable C IV absorption (Maran et al. 1996; Crenshaw et al. 1999). There was no detectable C IV absorption in the 1993 February GHRS spectrum, however, by 1995 April, two kinematic components appeared, at radial velocities of -1365 km s^{-1} (referred to as component 1) and -548 km s^{-1} (component 2) relative to the systemic redshift (we adopt $z = 0.009760 \pm 0.000093$ throughout this paper; de Vaucouleurs et al. 1991). Additionally,

a GHRS spectrum of the N V $\lambda\lambda 1239,1243$ spectral region revealed absorption coincident in velocity with component 2 just 16 days after the 1993 February observation of C IV that showed no absorption, suggesting rapid variability (Lu et al. 1994). A Space Telescope Imaging Spectrograph (STIS) medium resolution echelle spectrum of NGC 3783 was obtained on 2000 February 27 revealing a third kinematic component in C IV ($v_r = -724 \text{ km s}^{-1}$, component 3), in addition to the components seen in the final GHRS spectrum (Kraemer et al. 2001a). Ly α and N V $\lambda\lambda 1239,1242$ also appeared in these three kinematic components in the STIS spectrum. Si IV $\lambda\lambda 1394,1403$ absorption was only found in component 1 and no lines from lower ionization species, i.e., C II, Si II, Mg II, were detected. Using the N V doublet lines, Kraemer et al. (2001a) found that all three absorption systems have a non-unity effective covering factor. No correlation was found between the strength of the UV absorption features and continuum flux in the GHRS and STIS spectra by Kraemer et al. (2001a). They concluded the observed absorption variations were due largely to a change in total column. However, it was not possible to constrain tightly the variation timescales due to the sampling of these observations. Additionally, these observations did not sample the rapid changes in the continuum flux that were observed in the study by Reichert et al. (1994), thus, it remains unclear what affect variable ionization has on the absorption.

A large ($> 10^{22} \text{ cm}^{-2}$) and variable column of ionized gas was measured in the X-ray spectrum of NGC 3783 with the *Advanced Satellite for Cosmology and Astrophysics (ASCA)* (e.g., George et al. 1998). Subsequent observations with the High Energy Transmission Grating Spectrometer (HETGS) aboard the *Chandra X-ray Observatory (CXO)* showed numerous absorption lines with a mean radial velocity of $\sim -610 \pm 130 \text{ km s}^{-1}$, consistent with components 2 and 3 identified in the UV (Kaspi et al. 2000, 2001). The coincidence in velocities suggests a link between the UV and X-ray absorbers. Photoionization modeling of the STIS spectrum revealed that, although the UV absorbers can produce some of the observed X-ray columns, the ionization is too low and the total column too small to account for all of the features in the X-ray (Kraemer et al. 2001a). Hence, the exact relationship of the UV and X-ray absorption remained uncertain. Additionally, Kraemer et al. (2001a) found that two zones are required to explain the UV absorption columns measured in component 1. The strength of the Si IV absorption is inconsistent with the large N V/C IV column density ratio measured in the STIS spectrum. They proposed a model where a relatively high density absorber is co-located with more tenuous gas that is more highly ionized.

Various studies of intrinsic absorption in AGNs have demonstrated the importance of determining the absorption covering factor in the line-of-sight to the nucleus. In addition to affecting column density measurements, the covering factor constrains the absorption and emission geometry, providing tests for physical models. Non-unity effective covering factors, C_f , can arise from scattering of light into our line-of-sight by an extended scatterer (e.g., Cohen et al. 1995; Goodrich & Miller 1995; Kraemer et al. 2001b) or partial occultation of the emission sources (Wampler et al. 1993; Barlow & Sargent 1997; Hamann et al. 1997). In the most general case, the different covering factors of the continuum and emission-line region need to be determined (Barlow & Sargent 1997; Ganguly et al. 1999), and C_f can vary across the profile of an individual absorption component (e.g., Barlow et al. 1997; Arav et al. 2002). Additionally, instrumental scattering can affect the derived C_f and column densities (Crenshaw et al. 1998). High-resolution spectra with high signal-to-noise (S/N) are required to separate these effects.

We have undertaken an intensive multiwavelength monitoring campaign to probe the intrinsic absorption in NGC 3783 using observations in the UV, far-UV, and X-ray. In this paper, we present an analysis of the averaged spectrum in the UV and far-UV from STIS and the *Far Ultraviolet Spectroscopic Explorer (FUSE)*. We have co-added all observations to produce a high S/N spectrum that samples numerous lines from a range of ionization states. Analysis of the mean X-ray spectrum is presented in Kaspi et al. (2002),

hereafter Paper I. Details of the variable nature of the absorption will be presented in future papers by Gabel et al. (in preparation) and George et al. (in preparation). This paper is organized as follows: in §2, we present details of the *STIS* and *FUSE* observations and data reduction; in §3, measurements of the covering factors and column densities for the UV absorbers are given; in §4 we derive constraints on the physical conditions and geometry of the absorbers; we summarize our results in §5.

2. Observations, Data Reduction, and the UV – Far-UV Spectrum

The nucleus of NGC 3783 was observed with *HST/STIS* at 18 epochs between 2000 February 27 to 2002 January 6, and with *FUSE* at 5 epochs between 2001 February 28 to 2001 June 30. Each *STIS* medium-resolution echelle spectrum was obtained in two orbits through the $0''.2 \times 0''.2$ aperture centered on the nucleus using the E140M grating, which covers 1150-1730 Å. Exposure times and observation dates are given in Table 1. All spectra were reduced using the IDL software developed at NASA Goddard Space Flight Center for the Instrument Definition Team. We incorporated a procedure to remove the background light from each order using a scattered light model devised by Lindler (1999). Each echelle spectrum was generated by averaging together the individual orders in regions of overlap. The extracted *STIS* spectra are sampled in $\sim 5 \text{ km s}^{-1}$ bins. We measured residual fluxes in the cores of saturated Galactic lines in the *STIS* spectra ($\text{Ly}\alpha$, O I $\lambda 1302$, C II $\lambda 1335$, Si II $\lambda 1527$) to test the accuracy of the removal of scattered light. We find in all cases mean flux levels measured over the cores are consistent with zero within the noise levels. Typical values for the mean fluxes in the cores are $\pm 0\text{--}3\%$ of the local continuum flux, compared to uncertainties due to noise (i.e., the standard deviations measured over these intervals) of $\sim 5\text{--}12\%$ of the local continuum flux.

The *FUSE* spectra, which cover 905-1187 Å, were obtained in time-tag mode with the $30'' \times 30''$ low-resolution aperture (LWRS). Each observation consists of multiple exposures obtained in consecutive orbits on four detector segments, with two spectra (from the SiC and LiF channels) on each segment. Details of the observations are given in Table 2. Using IDL software obtained from the *FUSE* data analysis web page (<http://fuse.pha.jhu.edu/analysis/analysis.html>), we examined each raw two-dimensional image for instrumental effects that may contaminate the data. Numerous “event bursts” were found (see discussion in Oegerle et al. 2000) and an instrumental artifact affects the long wavelength region of all LiF 1B spectra. This artifact, known as “the worm”, is due to shadowing by one of the grid wires above the detector (Oegerle et al. 2000). The raw data were screened to remove these effects and processed using the standard *FUSE* calibration pipeline, CALFUSE v1.8.7.

CALFUSE extracts eight one-dimensional spectra for each exposure, corresponding to the two channels and four detector segments. Since the extracted *FUSE* spectra are oversampled, we rebinned to $8 \text{ km s}^{-1} \text{ bin}^{-1}$ to achieve higher S/N while preserving the full instrumental resolution (one resolution element corresponds to two data bins), which is nominally $\sim 20 \text{ km s}^{-1}$ (Oegerle et al. 2000). For each channel/segment, we compared the wavelength scales for all exposures using cross-correlation and corrected for any offset. All exposures were then co-added, weighted by exposure time. To achieve the highest possible S/N, the resulting spectra for the eight channel/segments were also co-added. To correct for the non-linear shifts in wavelength scale in the detector segments, we cross-correlated and aligned the spectra over small bandpasses. The spectra were then co-added by weighting each channel/segment with its effective area, using the effective area versus wavelength functions given in Blair et al. (2000). The absolute wavelength scale was determined from the intrinsic wavelengths of the Galactic lines. We measured flux levels in the cores of saturated Galactic H_2 lines, and find they are consistent with zero within the noise of the data.

2.1. The Averaged UV – Far-UV Spectrum

The individual STIS and *FUSE* observations were co-added to produce an averaged spectrum for each instrument. We have tested the individual observations extensively and find that our results in this paper are not strongly sensitive to variability in the spectra. Specifically, we performed all measurements described in the subsequent analysis on each STIS and *FUSE* observation, as well as on various coadded combinations of the individual observations. We find that the measurements of the covering factors in §3.1 and §3.2 below are not affected by variability, within the uncertainties of those measurements. There are variations in column densities for some of the ions, and these will be given a full treatment in an upcoming paper (Gabel et al. [in preparation]). Thus, the column density measurements presented in §3.2 are average values.

In Figure 1, the spectra for the O VI+Ly β , Ly α +N V, C IV, and Si IV resonance lines are plotted. Wavelengths corresponding to four previously identified intrinsic absorption components are denoted with tick marks for each line. Components 1–3 are those identified in the initial STIS spectrum by Kraemer et al. (2001a). Component 4, at $v_r = -1027 \text{ km s}^{-1}$ in the rest frame of the host galaxy, was first identified in O VI and Ly β in an earlier *FUSE* spectrum (Kaiser & Kriss 2002; Gabel et al. 2002). We note that absorption in this component is weak or absent in all other lines and its detection is very sensitive to the fit to the intrinsic emission. Additionally, Galactic O VI $\lambda 1032$ absorption may contribute to the observed Ly β feature (this will be addressed further in a study of the Galactic absorption by Mathur et al. [in preparation]). Given these uncertainties, we consider component 4 to be a tentative detection of intrinsic absorption. Interstellar absorption lines and detector artifacts are also identified on the top of each spectrum in Figure 1. The local interstellar absorption includes three kinematic components, at 0, +60, and +240 km s^{-1} with respect to the Galactic rest frame (Lu et al. 1994).

We modeled the intrinsic continuum and emission line fluxes at each absorption feature in the following manner (“intrinsic” flux here refers to the AGN emission before passing through the absorbers). First, we modeled the intrinsic continuum *plus* emission-line flux by fitting a cubic spline to unabsorbed regions of the spectrum on either side of the line. Next, to determine the relative contribution of continuum and line emission at each absorption feature, we estimated the *continuum* flux levels at each absorption feature by measuring the flux in regions of the spectrum that are not affected by line emission and linearly interpolating between these regions. Due to heavy contamination of the Ly α and O VI spectral regions by Galactic absorption, we used the C IV emission-line profile as a template in fitting the intrinsic emission for these lines. Specifically, we subtracted our fit to the continuum flux from our fit to the total C IV emission spectrum to derive its emission-line profile. We then scaled this profile in flux, preserving its velocity, and added it to the continuum flux for Ly α and O VI to derive the fit to these lines. We find that the C IV line template does not fit the O VI emission profile fully; an additional, narrow emission component is required. We modeled this with a $\text{FWHM} = 350 \text{ km s}^{-1}$ Gaussian profile centered at the systemic velocity of NGC 3783. Since this narrow line region component does not appear in the emission-line profiles in the STIS spectrum, it likely arises in an extended region that is not fully covered by the $0''.2 \times 0''.2$ STIS aperture. The broad line region (BLR) emission from Ly β and higher order Lyman lines is negligible in the *FUSE* spectrum. We have generated comparison models using the photoionization code CLOUDY (Ferland et al. 1998) for typical conditions in BLR gas and find this is consistent with the predicted spectrum. Multiple absorptions of the higher order Lyman line photons followed by cascade produce an H I spectrum dominated by Ly α . Thus, the line emission that is absorbed by Ly β is high velocity O VI BLR emission. Our fits to the total (dashed line) and continuum (dot-dashed line) fluxes are plotted on the spectra in Figure 1. We have modeled the Galactic H₂ and H I absorption, using the parameters derived in Sembach et al. (2001) for the high velocity cloud component. The fits to O VI, Ly β and Ly α shown in Figure 1 include absorption by this model.

In Figure 2, we show the spectra of Ly β and O VII illustrating the kinematic link between the UV and X-ray absorption. The O VII profile is a combination of the four strongest lines from that ion in the mean *Chandra* spectrum (see Figure 10 in Paper I). The velocities of the four intrinsic UV absorption components are marked with tick marks above the spectra. Structure in the X-ray absorption profiles is revealed in the high S/N mean *Chandra* spectrum. In Figure 2, at least two kinematic components are apparent in the O VII profile, coinciding with UV components 1 and 2+3 (see discussion in §3.5 of Paper I). We cannot rule out the presence of O VII absorption in component 4 as well.

3. Measurements

We normalized all absorption features by dividing the averaged spectrum by our fits to the intrinsic emission (see §2.1). The normalized profiles are plotted as a function of radial velocity in Figure 3. The centroid velocities of the four intrinsic absorption components are marked with dashed vertical lines on each spectrum. These were derived from the N V absorption for components 1–3 and Ly β for component 4. We have marked interstellar lines and known detector artifacts (labeled with "art") with short tick marks in Figure 3. Qualitatively, the absorption in the merged STIS data is similar to the initial spectrum presented in Kraemer et al. (2001a). Ly α , N V, and C IV are strong in components 1–3, while Si IV is only detectable in component 1. The C IV λ 1551 line in component 3 is blended with C IV λ 1548 in component 1. The blue wing of N V λ 1242 component 1 is blended with the red wing of N V λ 1238 component 2.

In the *FUSE* spectrum, the O VI λ 1032 line is heavily contaminated with Galactic features, but it appears in all components in O VI λ 1038. The deep feature in the red wing of component 1 in O VI λ 1038 is a detector artifact. We detect absorption in the Lyman lines up to Ly ϵ in components 1–3. Higher order Lyman lines may be present, but suffer from severe blending with Galactic absorption. Additionally, strong Galactic absorption contaminates component 1 in Ly γ and component 2 in Ly ϵ . In the top window of Figure 3a, Ly β is seen to be deeper than Ly α in components 1, 3, and 4, despite having an optical depth that is six times smaller. Additionally, the depth of Ly ϵ in components 1 and 3 indicates Ly β is saturated in these components since $\tau_\beta/\tau_\epsilon = 11$, but the residual flux levels in the cores of the Ly β features are non-zero. These are signatures of a complex absorption geometry in NGC 3783, which is addressed further in §3.1. Both N III λ 989 and N III* λ 991, which arises from the fine-structure level, are strong in component 1. The N III λ 989 component 1 profile shown in Figure 3c exhibits a sharp edge in the blue wing and spiked core blueward of the centroid. These features are not seen in the profiles of any other lines in this component, most notably the N III* λ 991 line. Furthermore, there is a strong Galactic H₂ line at this wavelength contaminating the N III absorption. Thus, this spike is likely due to noise in the deep trough of the H₂ + N III absorption. Weak absorption is also detected in components 2 and 3 in the N III* λ 991 line. C III λ 977, also predicted to be strong in component 1 (Kraemer et al. 2001a), is heavily blended with Galactic H₂ and cannot be measured. However, the C III* $\lambda\lambda$ 1175–76 multiplet, which arises from metastable levels 6.5 eV above ground, is detected in the STIS spectrum, indicating high density in this component (Bromage et al. 1985). To our knowledge, this is the first detection of C III* $\lambda\lambda$ 1175–76 absorption in a Seyfert galaxy other than NGC 4151. Weak C III λ 977 absorption also appears in components 2 and 3. There is a weak feature corresponding to the P V λ 1118 line at the velocity of component 1. However, we cannot confirm the presence of this component in the other line of the doublet, P V λ 1128, due to contamination with Galactic absorption. The S VI $\lambda\lambda$ 933,944 resonance doublet is contaminated with Galactic interstellar features for all components and cannot be measured. Lines of lower ionization, such as C II and Si II, are not detectable in the spectrum.

3.1. Covering Factor Analysis of the Lyman Lines

The observed absorption depths are determined by a combination of the effective covering factor and the optical depths of the lines. The absorption must be properly corrected for C_f before an accurate column density can be measured. In general, the different covering factors of the line and continuum sources, C_f^l and C_f^c , must be taken into account. Following the method of Ganguly et al. (1999), we assume the same column of gas obscures the two emission sources, i.e., $\tau_l = \tau_c$. The observed residual flux in any absorption line is then given by

$$F = F_l(C_f^l e^{-\tau} + 1 - C_f^l) + F_c(C_f^c e^{-\tau} + 1 - C_f^c), \quad (1)$$

where F_l and F_c are the intrinsic line and continuum fluxes, respectively. Dividing equation 1 by $F_l + F_c$ gives the expression for normalized flux,

$$I = R_l(C_f^l e^{-\tau} + 1 - C_f^l) + R_c(C_f^c e^{-\tau} + 1 - C_f^c), \quad (2)$$

where $R_l = F_l/(F_l + F_c)$ and $R_c = F_c/(F_l + F_c)$, which represent the relative contributions of line and continuum emission to the total intrinsic flux.

The Lyman lines provide a unique study of the covering factor. They give a set of lines that (a) span a large range in optical depth and (b) have substantially different relative contributions from continuum and line emission, R_c and R_l . Since they arise from the same atomic energy level, their optical depths scale simply by their $f\lambda$ ratios, where f is the oscillator strength and λ the laboratory wavelength of the lines. In Figure 3a, the strong absorption in the cores of components 1 and 3 in Ly ϵ , and component 2 in Ly γ (Ly ϵ is blended with Galactic C I in this component) indicates both Ly α and Ly β are saturated in these components and, therefore, *their core absorption depths are determined entirely by the covering factor*. Since Ly α and Ly β are saturated, $e^{-\tau} \approx 0$ for these two lines and their normalized flux given by equation 2 reduces to a simple function of C_f^l and C_f^c . We have combined these simplified equations for Ly α and Ly β and solved for C_f^l and C_f^c in the cores of the absorption, thereby separating the individual covering factors of the line and continuum sources. In these measurements, we averaged over 50 km s⁻¹ intervals centered on the centroid velocities of the components. We note that this analysis assumes the C_f^l of the O VI emission (which affects the Ly β absorption profile) and the Ly α emission are identical.

In Table 3, we list the normalized residual flux, I , and the fractional contribution of continuum emission to the total intrinsic flux, R_c , measured in the core of each available Lyman line, along with our derived values for C_f^l and C_f^c . The 1 σ uncertainties quoted in Table 3 were computed from repeated measurements using different placements of intrinsic continuum and BLR flux levels, and include the uncertainty in the residual flux due to noise. These results show the discrepancies in the apparent absorption strengths seen in Figure 3a are due to different covering factors of the line and continuum sources. For example, in component 1 where the Ly β absorption is deeper than Ly α , $R_c = 0.57$ and 0.15 for Ly β and Ly α , respectively, indicating $C_f^l < C_f^c$ in this component.

A closer look at the Lyman profiles in Figure 3a reveals the absorption in the higher order lines is resolved in the individual kinematic components, and is deep over several resolution elements in the *FUSE* data. Thus, we extended the above analysis to derive the line and continuum covering factors as a function of radial velocity. An exact solution to C_f^l and C_f^c is obtained at all radial velocities where Ly β is saturated. Since the optical depths of the Lyman lines scale according to their $f\lambda$ ratios, this can be determined from the strengths of the higher order Lyman lines. In general, $I \geq e^{-\tau}$, where the $>$ in the relation applies if the covering factor is less than unity. Thus, the velocities where $(I_{LyX})^{\tau_\beta/\tau_X}$ equals zero within uncertainties gives a conservative estimate of the regions of saturated Ly β (X represents ϵ for components 1 and 3 and

γ for component 2). For velocities where $\text{Ly}\beta$ is not saturated, such as in component 4 and in the outer wings of the absorption in components 1–3, the solution gives only lower limits to C_f^l and C_f^c . In Figure 4, the derived covering factor profiles are plotted. Velocities with only lower limits on the covering factors are plotted with a dotted line. Figure 4a shows that the continuum covering factor decreases smoothly in the blue wings of components 1 and 3, at velocities where the covering factor is well determined (solid line). Thus, the decreased absorption observed in these wings in $\text{Ly}\beta$ (Figure 3a) is a result of decreasing coverage of the continuum source, and the profile shape traces out the unocculted flux. The other absorption wings may also exhibit decreased covering factor, however, only lower limits are available at these velocities. As discussed in Ganguly et al. (1999), instrumental smearing can introduce an error into computations of the covering factor profiles, particularly in the wings. To test this effect, we convolved the observed absorption profiles with the line spread function of *FUSE*. We find that the changes in the profiles are undetectable within the noise of the data, and conclude that instrumental smearing has a negligible effect on our results. The variable covering factor detected in this analysis indicates there is substructure in the individual absorbers and may provide a constraint on physical models of the absorption gas. This is addressed further in §4.

One possible source of error associated with our calculations that is not included in the uncertainties quoted in Table 3 is if the covering factor of the O VI and $\text{Ly}\alpha$ BLRs are not the same. The intensive *IUE* monitoring campaign of NGC 3783 showed the $\text{Ly}\alpha$ BLR flux variations lagged the continuum variations by 3.6 days, while the He II BLR flux lag was only 1.3 days (Onken & Peterson 2002), indicating the higher ionization line emission is located closer to the ionizing source. If the O VI BLR is also more compact than $\text{Ly}\alpha$, then C_f^l for $\text{Ly}\beta$ may be greater than $\text{Ly}\alpha$, leading to an overestimate of the continuum covering factor. This may explain the discrepancy in Figure 4a, where the continuum covering factor derived at velocities just blueward of the centroid in component 1 and in the core of component 4 is greater than unity.

Another possible source of error involves the contribution of light from an extended scattering region to the residuals in the absorption features. If the scattered light profile underneath the absorption has structure, this will affect the covering factor calculations (e.g., see Kraemer et al. 2001b). This has consequences in using limits on the size of the emission sources to constrain the size of the absorbers for cases of partial coverage. However, it seems unlikely that scattered light can explain all of the non-unity covering factors derived from the H I absorption. For example, to account for all of the residual flux in the cores of $\text{Ly}\alpha$ in components 1 and 3 would require that 60% and 50%, respectively, of the intrinsic continuum plus BLR flux is scattered light. We conclude that, at least in these cases, the low derived covering factors represent partial line-of-sight coverage of the emission-line source. Thus, large variations occur in C_f^l between the cores of the different components, with values decreasing for higher blueshifted radial velocities in components 1–3. We note that unobscured NLR emission cannot account for the low line covering factors, since the low C_f^l values occur at high outflow velocities. At most, the NLR only affects the red-wing of the lowest velocity component. Furthermore, it is difficult to see how the scattered light profile could explain the dramatic variation in the continuum covering factor derived in the blue wings of components 1 and 3. In the outer velocities of the wings, the scattered contribution would have to account for 60–70% of the total intrinsic flux. Thus, although we cannot rule out that the continuum source is fully occulted by the absorber in the cores of all the components, the decreasing covering factor derived in the *wings* of components 1 and 3 implies velocity-dependent, partial coverage of the continuum source.

3.2. Column Density Measurements

For doublet line absorption, the effective covering factor, which is a combination of the individual line and continuum covering factors, can be derived directly from the residual fluxes in the two lines using their intrinsic optical depth ratio (Hamann et al. 1997). However, many of the doublets in NGC 3783 are too heavily contaminated with other absorption to apply this technique. In these cases and for lines not arising from doublets, another measure of C_f is required that accounts for the individual line and continuum covering factors, as highlighted in our analysis of the Lyman lines. This is evident in component 1, in which $C_f = 0.63$ is measured in the core of N V using the doublet method, but C IV and O VI have only one measurable line. Figure 3 shows the O VI, C IV, and Ly α absorption depths are all relatively shallow compared to N V in this component. Our fits to the continuum and line emission reveal they also have a stronger relative contribution of BLR emission at the wavelengths of component 1 absorption ($R_l = 0.74, 0.82,$ and 0.85 for O VI, C IV, and Ly α , respectively, compared to $R_l = 0.58$ for N V). In § 3.1, we found the Ly α absorption is saturated but it appears weak because of a low covering factor of the BLR. Similarly, the shallow absorption observed in O VI and C IV may also be the result of relatively low effective covering factors rather than low column densities. This was suggested by the photoionization modeling results of Kraemer et al. (2001a), which showed that substantial columns of C IV and/or O VI should always accompany a large N V column.

Motivated by these results, we used the covering factors for H I to derive effective covering factors and column densities for all intrinsic absorption lines. Following Ganguly et al. (1999), the effective covering factor is defined in terms of the individual line and continuum covering factors,

$$C_f = R_l C_f^l + R_c C_f^c. \quad (3)$$

For each line, we computed C_f as a function of radial velocity from the C_f^c and C_f^l profiles derived for H I and our fits to the intrinsic continuum and line fluxes. The effective covering factors, averaged over 50 km s $^{-1}$ intervals in the cores of the absorption components, are listed in Table 4. Uncertainties were derived by propagating the errors associated with C_f^c and C_f^l . For the doublet absorption in which the cores of both lines are uncontaminated with other absorption, i.e., Si IV component 1 and N V components 1–3, we also computed the effective covering factors in the cores of the absorption directly using the doublet method as described in Hamann et al. (1997). These values, and associated uncertainties, are listed in parentheses in Table 4. These results show the effective covering factor derived for H I in component 1 is equivalent to that determined for N V, but is larger than the Si IV covering factor by more than a factor of two. *This provides the only evidence for a covering factor within an individual kinematic component that is a function of ionization.* We note this may indeed be the case since component 1 likely consists of at least two distinct subcomponents, one of which is lower ionization and responsible for all of the Si IV absorption Kraemer et al. (see 2001a). Comparison of the line widths in this component reveals further evidence of substructure. In Table 5, we give the FWHM and centroid velocities measured directly from the normalized absorption profiles for each line in component 1. The Si IV and N III* lines are significantly narrower than the higher ionization lines, N V and C IV.

Substituting equation 3 into equation 2 gives the familiar expression for normalized flux as a function of the effective covering factor (Hamann et al. 1997),

$$I = C_f e^{-\tau} + 1 - C_f. \quad (4)$$

The factor $1 - C_f$ in equation 4 is the normalized unocculted flux. This represents the fraction of the total intrinsic flux that is unobscured by the absorber. The normalized absorption profiles for O VI, N V, C IV, and H I are plotted together with the normalized unocculted flux levels derived from equation 4 (dashed lines)

for component 1 in Figure 5a and components 2+3 in Figure 5b. In these figures we have plotted only the least contaminated line for the doublets. Figure 5 illustrates how the apparent absorption is a convolution of covering factor and column density. For lines with large column densities, the normalized flux will approach the unocculted flux level, but never lie below it (see equation 4). Other than the detector artifact in O VI $\lambda 1038$ component 1 (Figure 5a), we find no cases where residual fluxes lie below the unocculted flux levels outside the 1σ uncertainties. This supports the validity of using the H I covering factors.

In Figure 5, the absorption depths in several lines closely match the derived unocculted flux levels, indicating possible saturation in these lines. For example, the residual flux in the O VI $\lambda 1038$ feature in components 2 and 3 traces the unocculted flux levels over nearly the entire profile. The O VI $\lambda 1032$ absorption gives a consistent result in the narrow windows of component 2 that are uncontaminated with Galactic absorption ($v_r \approx -650$ and -450 km s $^{-1}$ in Figure 3b). Additionally, the absorption in the blue wings of N V $\lambda 1238$, C IV $\lambda 1548$, and O VI $\lambda 1038$ in component 1 appears saturated. However, the absorption is seen to diverge from the unocculted flux in the red wing of N V and C IV (O VI is contaminated with a detector artifact at these velocities). Thus, if the covering factor profiles derived for H I are valid for these lines, the column densities are not uniform across the profile in component 1, providing further evidence for substructure in this component. Given the uncertainties in the covering factor profiles due to the uncertain scattered light profile and the possibility that the covering factors of the O VI and Ly α BLRs are not the same, as described in § 3.1, we cannot rule out that this apparent substructure is due to our assumptions about the covering factor profiles.

Equation 4 can be rearranged to give the optical depth (Hamann et al. 1997),

$$\tau_v = \ln\left(\frac{C_f}{I - 1 + C_f}\right), \quad (5)$$

where the subscript indicates the calculation is made at each radial velocity, thereby giving the optical depth profile. The column density at each radial velocity is then obtained from the optical depth,

$$N_v = \frac{m_e c}{\pi e^2 f \lambda} \tau_v, \quad (6)$$

(Savage & Sembach 1991). We measured the total column density for each line by integrating equation 6 over the optical depth profiles calculated from equation 5; results are given in Table 6. For the doublets where a direct measurement of the effective covering factor is available from the residuals in the two lines, we used the core value listed in parenthesis in Table 4 to compute the column density. Components 2 and 3 were deblended following the method outlined in Kraemer et al. (2001a). In saturated regions, we measured lower limits for the column densities using $I + \Delta I$ in equation 5, where ΔI is the 1σ uncertainty in the normalized flux. Upper limits on undetectable lines were determined from uncertainties in the normalized fluxes. The 1σ uncertainties quoted in Table 6 were estimated from repeated measurements, and include uncertainties in our fits to the intrinsic emission as well as the photon noise. We note that the lower limits on the O VI columns from the combined components are consistent with the upper limit of 10^{17} cm $^{-2}$ derived from the X-ray spectrum in Paper I. If the P V absorption in component 1 is real (see discussion in §2), then it has a column density of $1.5 \pm 0.7 \times 10^{13}$ cm $^{-2}$.

Given the important implications of our results involving the covering factors, particularly the lower covering factor derived for Si IV, it is worthwhile to address the possible systematic errors that were discussed in §3.1 in more depth. First, we note that any contribution of scattered light to the residual fluxes in the Ly β or Ly α absorption will lead to an *underestimate* of the covering factors. This would lead to an even larger discrepancy between the effective covering factor derived for Si IV from the doublet and the prediction

from the H I results. The second possible systematic error is introduced if the sizes of the O VI and Ly α BLRs are not identical, leading to different emission line covering factors for Ly β and Ly α . Since the Ly ϵ absorption has no underlying BLR emission (see Table 3), it can be used to place limits on the covering factors that are unaffected by any discrepancy in the sizes of the BLRs of the different lines. For example, in component 1, an absolute lower limit on the H I *continuum* covering factor in the core follows directly from the depth of the feature, $C_f^c > 1 - I = 0.77$. This is strictly a lower limit, since (a) Ly ϵ is not saturated and (b) there may be a contribution from scattered flux. Using this result in equation 3, we derive an absolute lower limit on the effective covering factor predicted for Si IV from the H I covering factors, $C_f > 0.58$. Comparing this with the value derived from the Si IV doublet, $C_f = 0.30 \pm 0.07$, we conclude that our finding that the covering factor of Si IV is less than H I is robust.

4. Constraints on the Physical Conditions and Geometry of the Absorbers

While detailed photoionization modeling of the absorption will be presented in future papers (Kraemer et al. in preparation; Netzer et al. in preparation), we can place some immediate constraints on the physical conditions and geometry of the low ionization UV absorber in component 1. We refer to the photoionization modeling results in Kraemer et al. (2001a), which predicted a total hydrogen column density, $N_H = 5 \times 10^{18} \text{ cm}^{-2}$, and ionization parameter, $U = 0.0018$, for this subcomponent. Since the Si IV column measured in the averaged spectrum is somewhat higher than in the Kraemer et al. (2001a) study, partly due to the lower covering factor found for this line in the present study, and we have a more rigid upper limit on the C II column because of the high S/N, we have modified the models slightly. Using the ionizing spectral energy distribution and abundances employed in the models of Kraemer et al. (2001a), we find that $N_H \geq 10^{19} \text{ cm}^{-2}$ and $U \geq 0.005$ are required to match the Si IV column and C II upper limit simultaneously.

The detection of C III* $\lambda 1175\text{--}76$ absorption, which arises from metastable levels 6.5 eV above the ground state, implies a high density in the low ionization absorber in component 1 (Bromage et al. 1985; Kriss et al. 1992; Kraemer et al. 2001b). The relative population of the metastable levels is determined by the physical conditions in the absorber, and the ratio of metastable to ground state columns can be used to estimate the electron density, n_e (Kriss et al. 1992). Due to contamination of the C III $\lambda 977$ feature by Galactic H $_2$, the C III ground state column density cannot be measured directly in NGC 3783. Instead, we use the photoionization model results, which predict $N_{CIII} \approx 2 \times 10^{15} \text{ cm}^{-2}$. The predicted C III column is not a strong function of the exact U , N_H solution needed to match the Si IV, since Si IV and C III appear in the same zone due to the similarity in their ionization potentials. Our measured column for the metastable level from C III* $\lambda 1175\text{--}76$ ($1.2 \times 10^{13} \text{ cm}^{-2}$) then implies the ratio of metastable to ground state columns is ~ 0.006 . The photoionization models predict $T \approx 20,000 \text{ K}$ in the absorber, which is largely insensitive to the exact N_H , U solution for our assumed SED. Using the calculations in Kriss et al. (1992), this corresponds to $n_e \approx 10^9 \text{ cm}^{-3}$ for the low ionization subcomponent. This high density implies a very small radial dimension for the absorber, $\sim 10^{10} \text{ cm}$ for a column of 10^{19} cm^{-2} , which may indicate the gas is clumpy and has a low volume filling factor (see discussion below). From the density, lower limit on U , and estimate of the ionizing continuum luminosity given by Kraemer et al. (2001a), we derive an upper limit on the location of the absorber with respect to the ionizing continuum source, $R \leq 8 \times 10^{17} \text{ cm}$.

The partial coverage of the emission sources revealed in the analysis of the H I lines in § 3.1 also places constraints on the absorption geometry. At velocities exhibiting partial coverage, the area of the absorbing gas projected on the sky is smaller than the projected area of the emission sources. The monitoring study of NGC 3783 revealed large amplitude variations of both the continuum and BLR emission (Reichert et al.

1994; Onken & Peterson 2002). The most rigid constraint comes from the measured lag of the BLR flux variations behind the continuum variations. For example, Onken & Peterson (2002) found the Ly α BLR flux varied by up to a factor of 1.6 and lagged the continuum variations by 3.6 days. From light travel time arguments, this constrains the projected size of much of the BLR to be ~ 3.6 lt-days (10^{16} cm) across. Thus, in components 1 and 3, with $C_f^l = 0.31$ and 0.55 measured in the cores, the projected area of the absorbers is $\sim (5.5 \times 10^{15})^2$ and $\sim (7.5 \times 10^{16})^2$ cm², respectively.

These results provide important clues to the physical nature of the absorbers. The smoothly varying covering factor of the continuum detected in the wings of the absorption in §3.1 indicates there is substructure within the individual kinematic components. One interpretation of this result is that the absorption components are comprised of many small substructures, such as cloudlets or turbulent cells. In this scenario, the decreasing coverage in the wings may be a consequence of the velocity dispersion of these substructures, with a decreasing number of “clouds” having velocities that diverge from the centroid velocity. Since, in general, the ionic column densities do not decrease dramatically in the wings of the absorption profiles (see Figure 5), there cannot be much overlap of clouds in the cores of the absorbers, indicating they have small volume filling factors. The extreme compactness of the gas comprising the low ionization subcomponent in component 1 provides additional evidence for this model. Since the radial thickness of this gas is much smaller than the projected dimensions of the emission sources, the most natural explanation is that a large number of very small, dense clouds combine to give the observed absorption. The alternative interpretation would require that the absorber is an exceedingly thin sheet of material. Previous studies have invoked absorption by a clumpy gas to explain the complex structure seen in other AGN absorption systems (e.g., Hamann et al. 2001; Kriss 2002) and a highly inhomogeneous absorbing medium is predicted by the multitemperature wind models of Krolik & Kriss (2001).

5. Summary

NGC 3783 was observed with *HST*/STIS at 18 epochs and with *FUSE* at 5 epochs as part of an intensive multiwavelength monitoring campaign designed to investigate the intrinsic absorption in this Seyfert 1 galaxy. We have combined the observations to produce a high S/N averaged spectrum in the UV and far-UV. The major findings of our study follow.

1. O VI, N V, C IV, N III, and the Lyman lines up to Ly ϵ appear in the three kinematic components identified by Kraemer et al. (2001a) in the initial STIS spectrum (components 1, 2, and 3 at radial velocities -1320 , -548 , and -724 km s⁻¹, respectively). Galactic contamination prevents the detection of higher order Lyman lines. Si IV appears in component 1; C III $\lambda 977$ is heavily contaminated with Galactic absorption and cannot be measured in this component, but is present in components 2 and 3. We detect absorption from the C III* $\lambda 1175-76$ multiplet in component 1, indicating a high density in this absorber. This is the first detection of metastable C III in a Seyfert galaxy other than NGC 4151 (Bromage et al. 1985). No lower ionization lines appear in absorption, and we place stringent upper limits on their column densities. A fourth kinematic component of intrinsic absorption is tentatively identified at a radial velocity of -1027 km s⁻¹. This component appears strong only in Ly β , which may be contaminated with Galactic absorption, and O VI. In all other lines, the detection of this component is very sensitive to the fit to the intrinsic emission.

2. The Lyman lines reveal a complex absorption geometry in NGC 3783 and highlight the importance of determining the individual covering factors of the continuum and emission-line sources. The strength of the higher order Lyman lines indicates Ly α and Ly β are saturated in components 1–3. The continuum

and emission-line covering factors were separated using the Ly α and Ly β absorption in each kinematic component, both in the cores of absorption and as a function of radial velocity. The covering factor of the BLR varies significantly between the cores of the absorption components, with $C_f^l = 0.33, 0.84, 0.55,$ and 0.03 derived in components 1, 2, 3, and 4, respectively. The large residual fluxes measured in Ly α in components 1 and 3 imply that, at least in these components, the non-unity emission-line covering factors cannot be fully accounted for by light from an extended scatterer, and thus represent partial coverage of the BLR. We also find evidence for variation of the continuum covering factor with velocity in the individual kinematic components. Specifically, C_f^c decreases by $\sim 60\%$ over several resolution elements in the wings of the absorption. This smoothly decreasing coverage is a signature of substructure within the absorbers.

3. The individual continuum and line covering factors derived from H I were used to derive effective covering factors for all lines. Comparison to the covering factors derived directly by the doublet method reveals the Si IV covering factor is smaller than that of H I and N V by more than a factor of two in component 1. This implies substructure in component 1 and is consistent with the prediction by Kraemer et al. (2001a) that this component is comprised of at least two zones of UV absorption. Furthermore, the FWHM of Si IV and N III are narrower than the higher ionization lines in component 1, providing additional evidence for substructure. Employing the H I covering factor profiles for the higher ionization lines, we find the relatively weak apparent C IV and O VI absorption compared to N V in component 1 is due to low effective covering factors rather than small column densities. If the covering factors derived from H I are valid for C IV and N V, then the column densities of these lines are not uniform across the profile of component 1; they are saturated in the blue wing, but smaller in the red wing. Additionally, O VI is found to be saturated in components 2 and 3, as well as in the blue wing of component 1.

4. We place lower limits on the total hydrogen column density and ionization parameter in the low ionization subcomponent in component 1, $N_H \geq 10^{19} \text{ cm}^{-2}$ and $U \geq 0.005$. Combining model predictions of the total C III column with our measured C III* column gives $n_e \approx 10^9 \text{ cm}^{-3}$. These results imply an upper limit on the distance of the absorber from the ionizing continuum source of $\leq 8 \times 10^{17} \text{ cm}$. Using upper limits on the size of the BLR from the variability study by Onken & Peterson (2002), the projected area of the absorbers at velocities exhibiting partial coverage of the emission-line source is found to be $\sim (10^{16})^2 \text{ cm}^2$. The decreasing covering factor exhibited in the wings of the Lyman lines and extreme compactness of the C III* absorber are suggestive of a clumpy absorbing medium with a low filling factor.

J. R. G., D. M. C., and S. B. K. acknowledge support from NASA grant HST-GO-08606.13-A. W.N.B acknowledges CXC grant GO1-2103 and NASA LTSA grant NAG5-8107. F.H. acknowledges NSF grant AST 99-84040. We thank B-G Andersson and the *FUSE* team for assistance with the *FUSE* spectra and Derck Massa for providing his code for modeling the H₂ absorption. We also thank the anonymous referee for very helpful comments.

REFERENCES

- Arav, N., Korista, K. T., & de Kool, M. 2002, *ApJ*, 566, 699
- Barlow, T. A., & Sargent, W. L. W. 1997, *AJ*, 113, 136
- Barlow, T. A., Hamann, F., & Sargent, W. L. W. 1997, in *ASP Conf. Ser. 128, Mass Ejection from Active Galactic Nuclei*, ed. N. Arav, I. Shlosmann, & R. J. Weymann (San Francisco: ASP), 13
- Blair, W. 2000, *The FUSE Observers Guide, Version 2.1*
- Bromage, G. E., et al. 1985, *MNRAS*, 215, 1
- Cohen, M. H., Ogle, P. M., Tran, H. D., Vermeulen, R. C., Miller, J. S., Goodrich, R. W. & Martel, A. R. 1995, *ApJ*, 448, L77
- Crenshaw, D. M., Maran, S. P., & Mushotzky, R. F. 1998, *ApJ*, 496, 797
- Crenshaw, D. M., Kraemer, S. B., Boggess, A., Maran, S. P., Mushotzky, R. F., & Wu, C.-C. 1999, *ApJ*, 516, 750
- Crenshaw, D. M., & Kraemer, S. B. 1999, *ApJ*, 521, 572
- Crenshaw, D. M., Kraemer, S. B., Hutchings, J. B., Danks, A. C., Gull, T. R. Kaiser, M. E., Nelson, C. H., & Weistrop, D. 2000, *ApJ*, 545, L27
- de Vaucouleurs, G., de Vaucouleurs, A., Corwin, H. G., Buta, R. J., Paturel, G., & Fouque, P. 1991 *Third Reference Catalogue of Bright Galaxies* (Springer-Verlag: New York)
- Ferland, G. J., Korista, K. T., Verner, D. A., Ferguson, J. W., Kingdon, J. B., & Verner, E. M. 1998, *PASP*, 110, 761
- Gabel, J. R., Crenshaw, D. M., & Kraemer, S. B. 2002, in *ASP Conf. Ser. 255, Mass Outflow in Active Galactic Nuclei: New Perspectives*, ed. D. M. Crenshaw, S. B. Kraemer, & I. M. George (San Francisco: ASP), 81
- Ganguly, R., Eracleous, M., Charlton, J. C., & Churchill, C. W. 1999, *AJ*, 117, 2594
- George, I. M., Turner, T. J., Netzer, H., Nandra, K., Mushotzky, R. F., & Yaqoob, T. 1998, *ApJS*, 114, 73
- Goodrich, R. W., & Miller, J. S. 1995, *ApJ*, 448, L73
- Hamann, F., Barlow, T. A., Junkkarinen, V., & Burbidge, E. M. 1997, *ApJ*, 478, 80
- Hamann, F. W., Barlow, T. A., Chaffee, F. C., Foltz, C. B., & Weymann, R. J. 2001, *ApJ*, 550, 142
- Kaiser, M. E., & Kriss, G. A. 2002, in *ASP Conf. Ser. 255, Mass Outflow in Active Galactic Nuclei: New Perspectives*, ed. D. M. Crenshaw, S. B. Kraemer, & I. M. George (San Francisco: ASP), 75
- Kaspi, S., Brandt, W. N., Netzer, H., Sambruna, R., Chartas, G., Garmire, G. P., & Nousek, J. A. 2000, *ApJ*, 535, L17
- Kaspi, S., et al. 2001, *ApJ*, 554, 216
- Kaspi, S., et al. 2002, *ApJ*, 574, 643 (Paper I)

- Kraemer, S. B., Crenshaw, D. M., Gabel J. R. 2001a, *ApJ*, 557, 30
- Kraemer, S. B., et al. 2001b, *ApJ*, 551, 671
- Kriss, G. A., et al. 1992, *ApJ*, 392, 485
- Kriss, G. A. 2002, in *ASP Conf. Ser. 255, Mass Outflow in Active Galactic Nuclei: New Perspectives*, ed. D. M. Crenshaw, S. B. Kraemer, & I. M. George (San Francisco: ASP), 69
- Krolik, J. H., & Kriss, G. A. 1997, in *ASP Conf. Ser. 128, Mass Ejection from Active Galactic Nuclei*, ed. N. Arav, I. Shlosmann, & R. J. Weymann (San Francisco: ASP), 132
- Krolik, J. H., & Kriss, G. A. 2001, *ApJ*, 561, 684
- Lindler, D. 1999 *CALSTIS Reference Guide (CALSTIS Version 5.1)*
- Lu, L., Savage, B. D., & Sembach, K. R. 1994, *ApJ*, 426, 563
- Maran, S. P., et al. 1996, *ApJ*, 465, 733
- Oegerle, W., Murphy, E., & Kriss, G. A. 2000, *The FUSE Data Handbook, Version 1.1*
- Onken, C. A., & Peterson, B. M. 2002, *ApJ*, 572, 746
- Reichert, G. A., et al. 1994, *ApJ*, 425, 582
- Savage, B. D., & Sembach, K. R. 1991, *ApJ*, 379, 245
- Sembach, K. R., Howk, J. C., Savage, B. D., & Shull, J. M. 2001, *ApJ*, 121, 992
- Shields, J. C., & Hamann, F. 1997, *ApJ*, 481, 752
- Wampler, E. J., Bergeron, J., & Petitjean, P. 1993, *A&A*, 273, 15

Table 1. *HST*/STIS Observations of NGC 3783^a

Data Set	UT Start Time	Exp Time (seconds)
O57B01020 ^b	2000-02-27, 09:34:59	2700
O57B01030 ^b	2000-02-27, 11:11:33	2700
O63M01010	2000-08-05, 00:54:58	2200
O63M01020	2000-08-05, 02:18:41	2700
O63M02010	2000-11-26, 01:10:17	2200
O63M02020	2000-11-26, 02:35:18	2700
O63M03010	2001-01-25, 20:09:07	2200
O63M03020	2001-01-25, 21:34:05	2700
O63M04010	2001-02-25, 04:01:51	2200
O63M04020	2001-02-25, 05:22:57	2700
O63M05010	2001-02-28, 01:05:49	2200
O63M05020	2001-02-28, 02:28:43	2700
O63M06010	2001-03-02, 17:20:14	2200
O63M06020	2001-03-02, 18:43:59	2700
O63M08010	2001-03-11, 14:54:01	2200
O63M08020	2001-03-11, 16:20:48	2700
O63M09010	2001-03-15, 16:51:54	2200
O63M09020	2001-03-15, 18:19:14	2700
O63M10010	2001-03-19, 17:12:53	2200
O63M10020	2001-03-19, 18:40:08	2700
O63M11010	2001-03-23, 15:59:27	2200
O63M11020	2001-03-23, 17:24:31	2700
O63M12010	2001-03-27, 08:19:43	2200
O63M12020	2001-03-27, 09:43:10	2700
O63M14010	2001-04-04, 02:35:42	2200
O63M14020	2001-04-04, 03:57:29	2700
O63M15010	2001-04-08, 01:22:01	2200
O63M15020	2001-04-08, 02:41:30	2700
O63M16010	2001-04-11, 22:33:08	2200
O63M16020	2001-04-11, 23:49:35	2700
O63M07010	2001-04-16, 02:09:01	2242
O63M07020	2001-04-16, 03:28:27	2700
O63M53010	2001-04-23, 15:37:54	2242
O63M53020	2001-04-23, 17:02:53	2700
O63M17010	2002-01-06, 13:39:42	2242
O63M17020	2002-01-06, 15:15:51	2700

^aAll data obtained with the E140M echelle grating, through the $0''.2 \times 0''.2$ aperture.

^bData for this observation were presented in Kraemer et al. (2001a).

Table 2. *FUSE* Observations of NGC 3783^a

Data Set	UT Start Time	Exp Time (seconds)
B1070102000	2001-02-28, 16:46	27830
B1070106000	2001-03-07, 08:31	26400
B1070103000	2001-03-11, 12:56	27494
B1070105000	2001-03-30, 22:52	28099
B1070105000	2001-06-27, 05:26	27490

^aAll data obtained through the $30'' \times 30''$ LWRS aperture.

Table 3. Continuum and Emission-Line Covering Factors in the Cores of the Lyman Lines

Comp	I^a				R_c^b				$C_f^{c,c}$	$C_f^{l,c}$
	Ly α	Ly β	Ly γ	Ly ϵ	Ly α	Ly β	Ly γ	Ly ϵ		
1	0.57	0.27	...	0.23	0.15	0.57	0.92	1.0	1.0 (± 0.10)	0.31 (± 0.06)
2	0.18	0.20	0.38	0.50	0.10	0.52	0.89	1.0	0.74 (± 0.08)	0.84 (± 0.08)
3	0.41	0.26	0.24	0.46	0.11	0.52	0.90	1.0	0.9 (± 0.10)	0.55 (± 0.08)

^aResidual normalized flux in core measured over $\Delta v = -1325 - -1275$, $-575 - -525$, $-750 - -700$, and $-1050 - -1000$ km s⁻¹ for components 1, 2, 3, and 4 respectively.

^bFractional contribution of continuum to total intrinsic emission.

^cCovering factors of the continuum, C_f^c , and line, C_f^l , emission sources; quoted uncertainties do not include possible errors due to a contribution from scattered flux or structure in the BLR.

Table 4. Effective Covering Factors Derived in the Cores of Absorption Lines using H I^a

Line	Comp 1	Comp 2	Comp 3	Comp 4
O VI λ 1038	0.52±0.07	0.81±0.08	0.66±0.09	0.29
N V λ 1238	0.63±0.07 (0.63±0.04)	0.81±0.08 (0.61±0.05)	0.70±0.09 (0.66±0.04)	0.41
N III* λ 991	0.93±0.10	0.78±0.08	0.86±0.10	...
C IV λ 1548	0.45±0.07	0.82±0.08	0.60±0.08	0.19
C III λ 977	...	0.79±0.08	0.88±0.10	0.84
C III* λ 1775-76 ^c	0.88±0.10
Si IV λ 1393	0.72±0.07 (0.30±0.07)

^aCovering factors derived using C_f^l and C_f^c derived for H I; effective covering factors derived directly from doublet method are given in parenthesis. Values are averages measured over $\Delta v = -1325 - -1275$, $-575 - -525$, $-750 - -700$, and $-1050 - -1000$ km s⁻¹ for components 1, 2, 3, and 4 respectively.

Table 5. Kinematics in Absorption Component 1

Line	Velocity ^a km s ⁻¹	FWHM km s ⁻¹
N V λ 1238	-1304 (\pm 10)	194 (\pm 7)
C IV λ 1548	-1322 (\pm 10)	180 (\pm 7)
Si IV λ 1393	-1326 (\pm 15)	111 (\pm 10)
N III* λ 991	-1331 (\pm 20)	124 (\pm 15)
Ly β	-1297 (\pm 12)	219 (\pm 10)
Ly ϵ	-1315 (\pm 20)	145 (\pm 15)

^aCentroid velocity with respect to the systemic redshift of the host galaxy.

Table 6. Ionic Column Densities^a (10^{14} cm^{-2})

Ion	Component 1	Component 2	Component 3	Component 4
H I	140 (± 20)	37 (± 9)	163 (± 30)	5.0 (± 2.0)
O VI	>14	>12	>51	6.1 (± 4.0)
N V	>11	2.6 (± 0.5)	11.4 (± 2.0)	0.50 (± 0.4)
N III	4.4 (± 2.5)	<1.0
N III ^{*b}	4.5 (± 1.5)	0.4 (± 0.2)	1.5 (± 0.8)	<1.0
C IV	>4.5	0.60 (± 0.13)	2.6 (± 0.5)	0.34 (± 0.25)
C III	...	0.30 (± 0.2)	0.90 (± 0.35)	...
C III ^{*c}	0.12 (± 0.06)	<0.05	<0.03	<0.03
C II	<0.6	<0.25	<0.10	<0.10
Si IV	0.89 (± 0.20)	<0.1	<0.03	<0.03
Si II	<0.06	<0.04	<0.02	<0.01

^aCovering factors derived for H I were used in all measurements, except where direct measurement of C_f using the doublet method was possible; ... denotes no measurement available due to blending with other features; lower limits given for saturated lines.

^bPopulation of N^{+1} J=3/2 fine-structure level.

^cPopulation of C^{+2} $^3\text{P}^o$ metastable levels (6.5 eV).

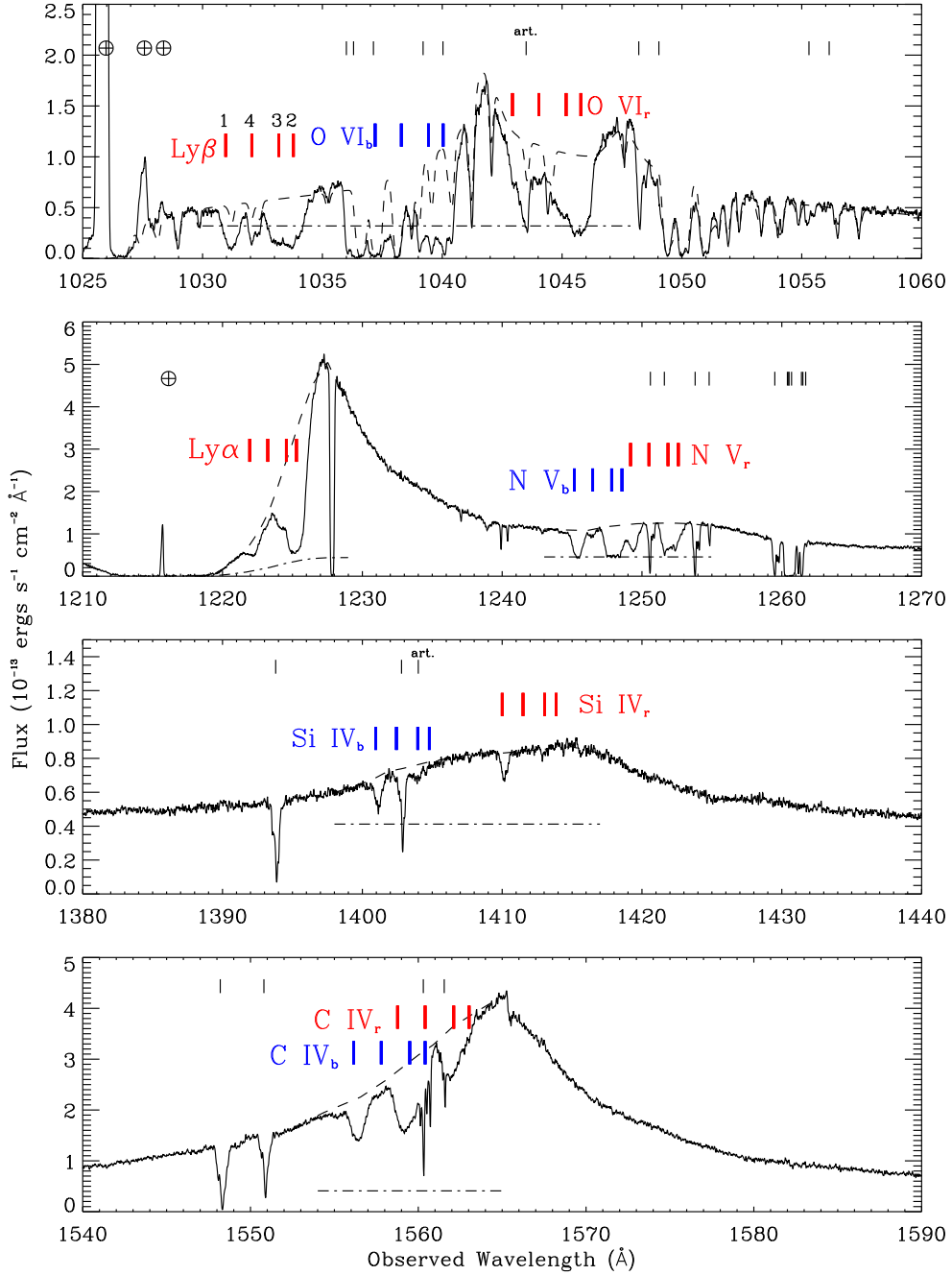


Fig. 1.— Portions of the averaged STIS and *FUSE* spectrum of NGC 3783 showing intrinsic absorption. Wavelengths corresponding to the four detected absorption components are identified with red and blue tick marks. Labels showing our numbering of the components are given above Ly β . Fits to the intrinsic continuum plus line emission are plotted over each line (dashed). Continuum flux levels are plotted as dot-dashed lines. The fit to the total intrinsic flux for O VI, Ly β and Ly α includes our model of the Galactic H₂ and H I absorption. Other strong interstellar lines and detector artifacts (labeled with "art.") are denoted with short tick marks at the top of each spectrum. Geocoronal emission lines are labeled with \oplus symbols.

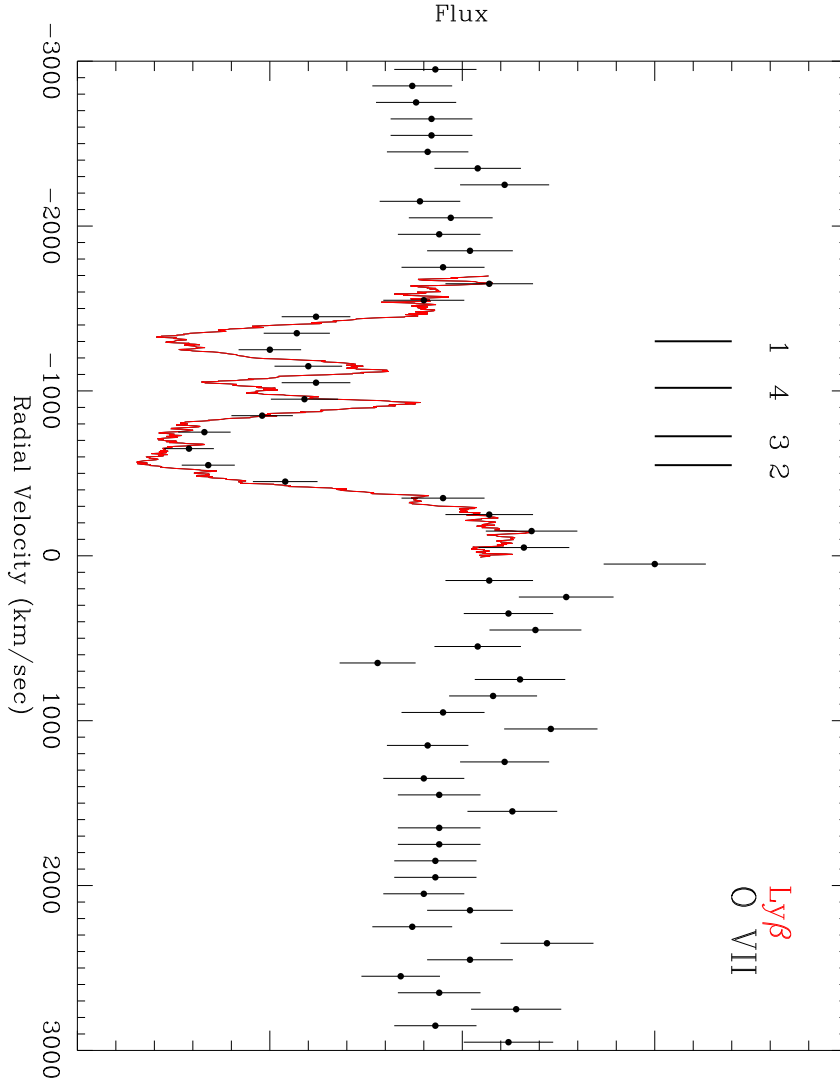


Fig. 2.— Spectra of Ly β and O VII showing the kinematic link between the UV and X-ray absorption in NGC 3783. The data are plotted in arbitrary flux units. The Ly β data (red line) are from the averaged *FUSE* spectrum. The O VII profile is a combination of the four strongest lines from that ion in the averaged *Chandra* spectrum (see §3.5 in Paper I); these data are binned at 100 km s⁻¹. Each line is plotted as a function of radial velocity with respect to the systemic redshift. The velocities of the four kinematic components are marked with tick marks above the spectra. As described in Paper I, structure is apparent in the O VII profile, coinciding in velocity with the UV components.

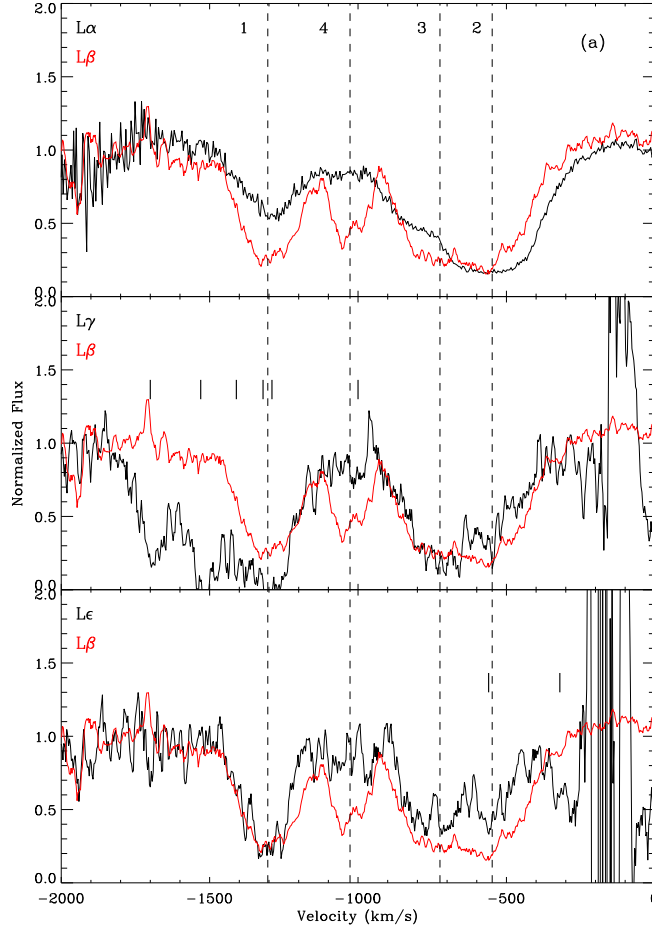


Fig. 3.— Normalized profiles of lines exhibiting intrinsic absorption in NGC 3783. The spectra are plotted as a function of radial velocity with respect to the systemic redshift. Centroid velocities of the four kinematic absorption components are marked with dashed vertical lines. These were derived from the N V $\lambda 1239$ profile for components 1–3, and Ly β for component 4. Short tick marks identify strong interstellar lines and detector artifacts (labeled with "art.") in each spectrum. In 3a, Ly β (red line) is plotted together with Ly α , Ly γ , and Ly ϵ . In 3b, the short wavelength (blue line) and long wavelength (red line) members of the doublets are plotted together. The tick marks identifying Galactic lines in 3b are color coded to the corresponding line of the doublet. In the second panel in 3c, the C III* spectrum is plotted with respect to the shortest wavelength line in the multiplet. The positions of the six multiplet lines for component 1 are marked with long tick marks at the top of the spectrum. In the N III $\lambda 989$ spectrum (third panel in 3c), component 1 N III* $\lambda 991$ absorption is marked with a thick tick mark and labeled. Tentative absorption is detected in P V $\lambda 1118$ in component 1 (bottom panel in 3c), however this cannot be confirmed in the P V $\lambda 1128$ line due to contamination by Galactic absorption. All profiles have been corrected for Galactic H₂ and H I absorption. Regions with large fluctuations in the normalized flux are where saturated interstellar lines were divided out.

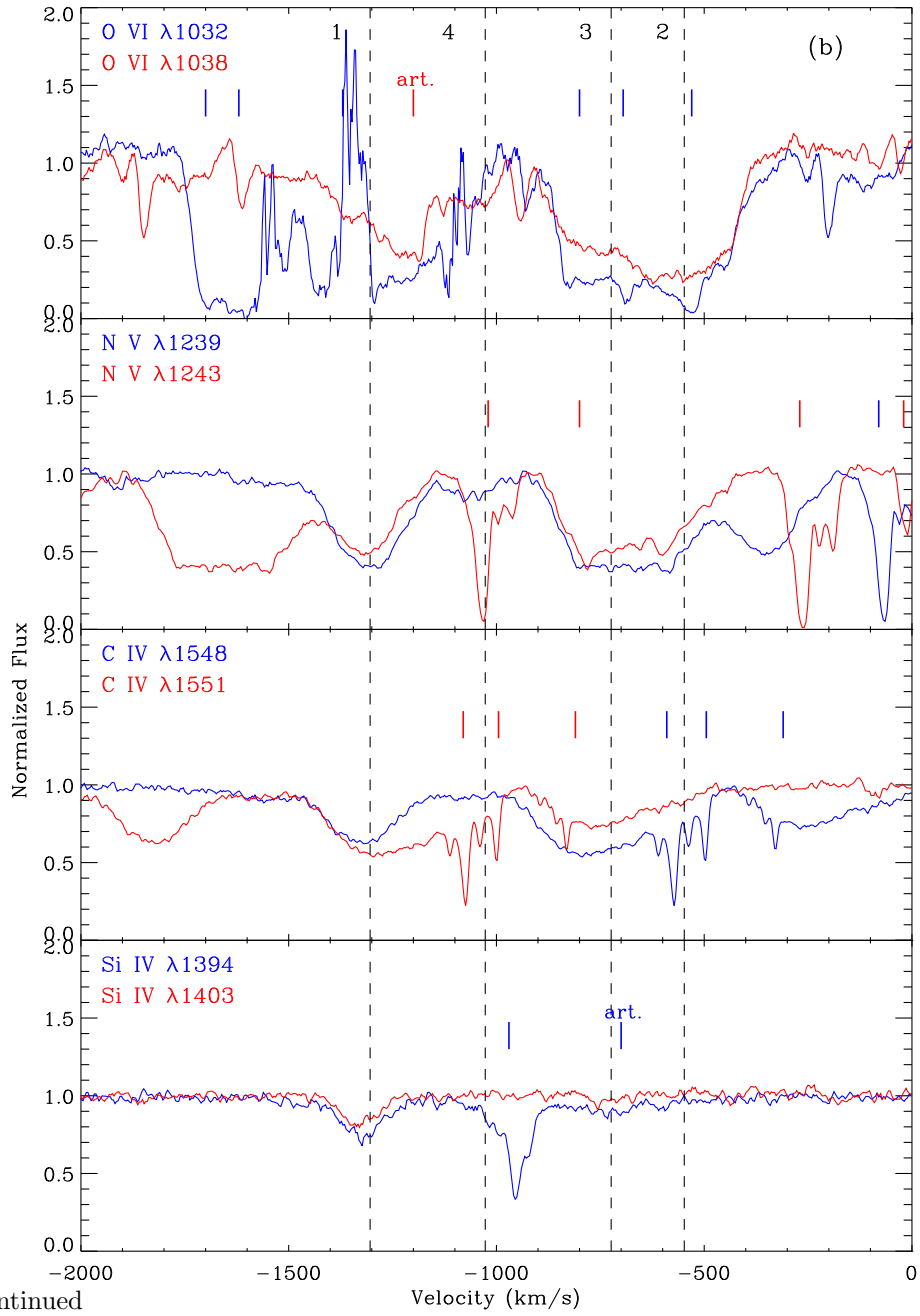


Fig. 3.— Continued

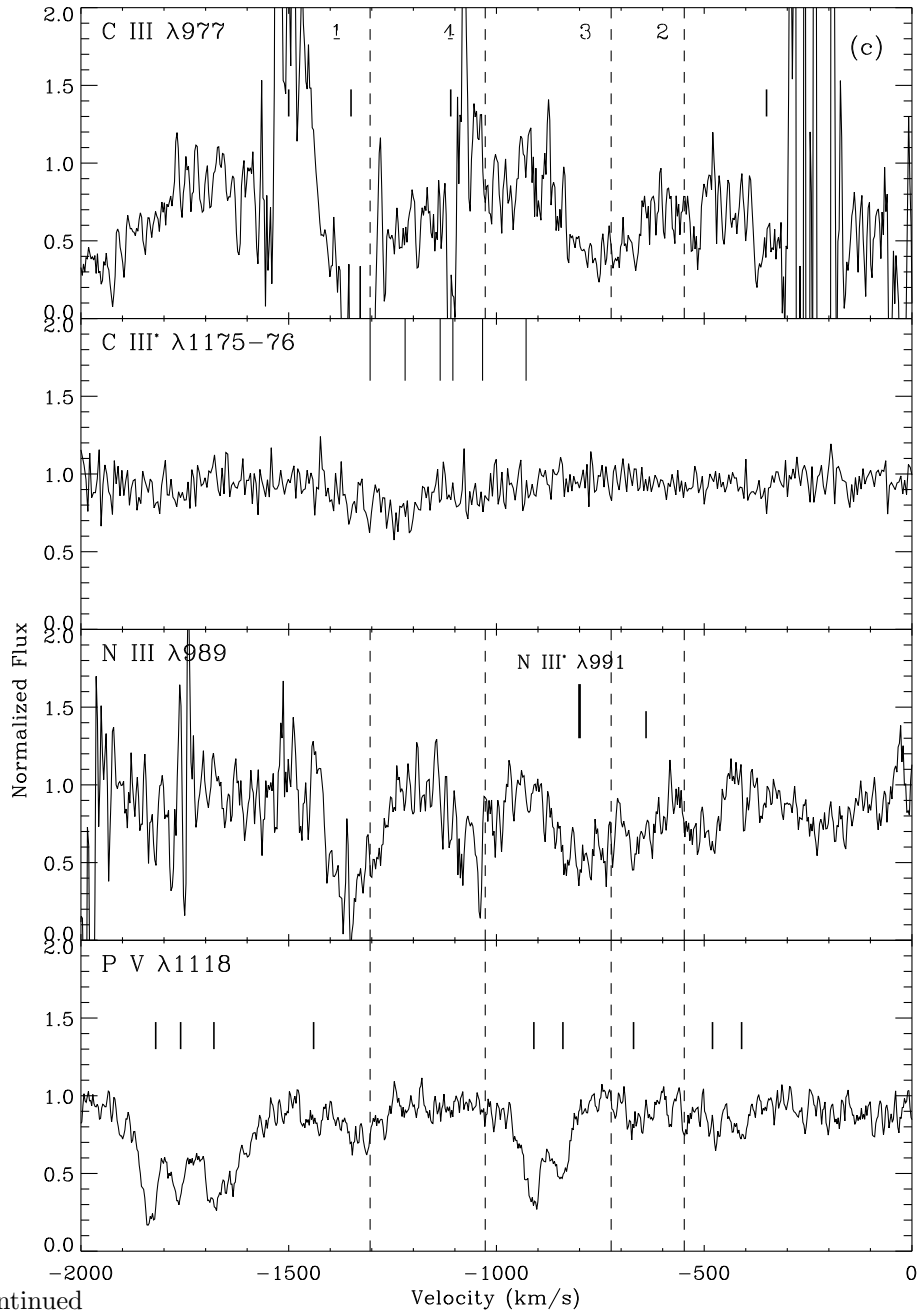


Fig. 3.— Continued

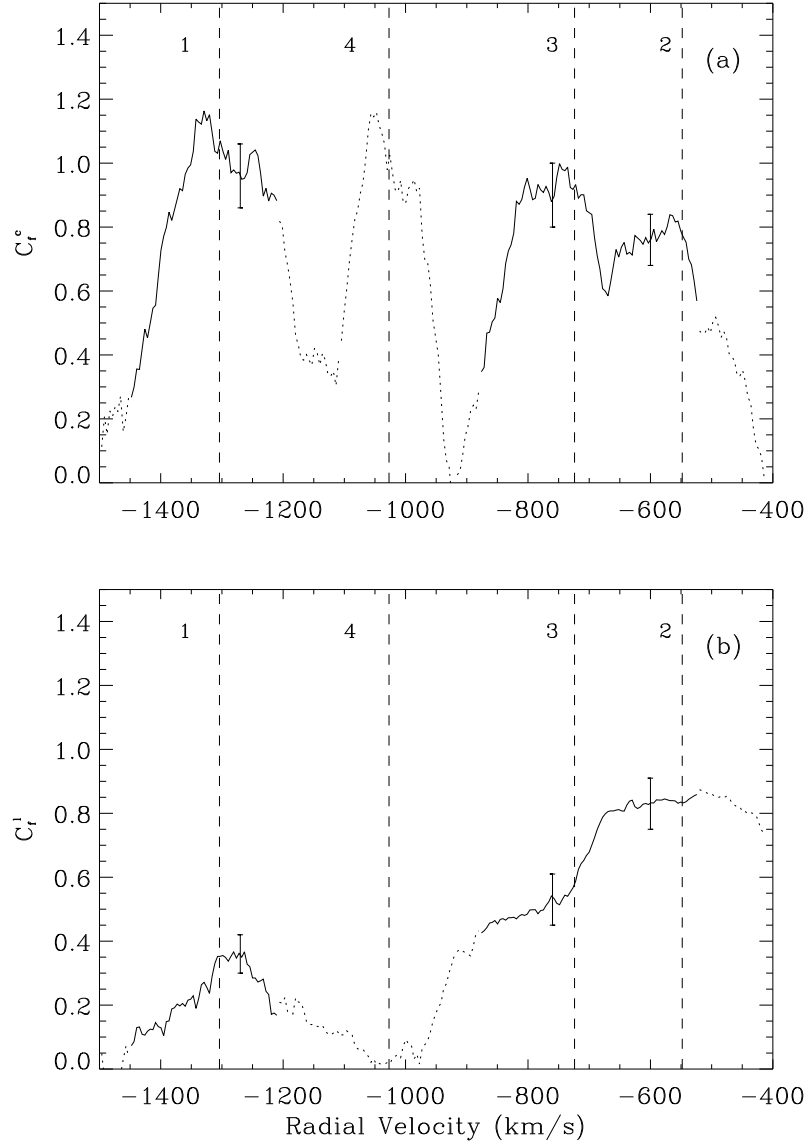


Fig. 4.— Covering factor as a function of radial velocity derived for H I for the continuum (4a) and emission-line region (4b). The dotted line represents lower limits to C_f^c and C_f^l , where Ly β is not saturated. Centroid velocities of the four kinematic absorption components are marked with dashed vertical lines. Sample error bars are included in the cores of components 1–3.

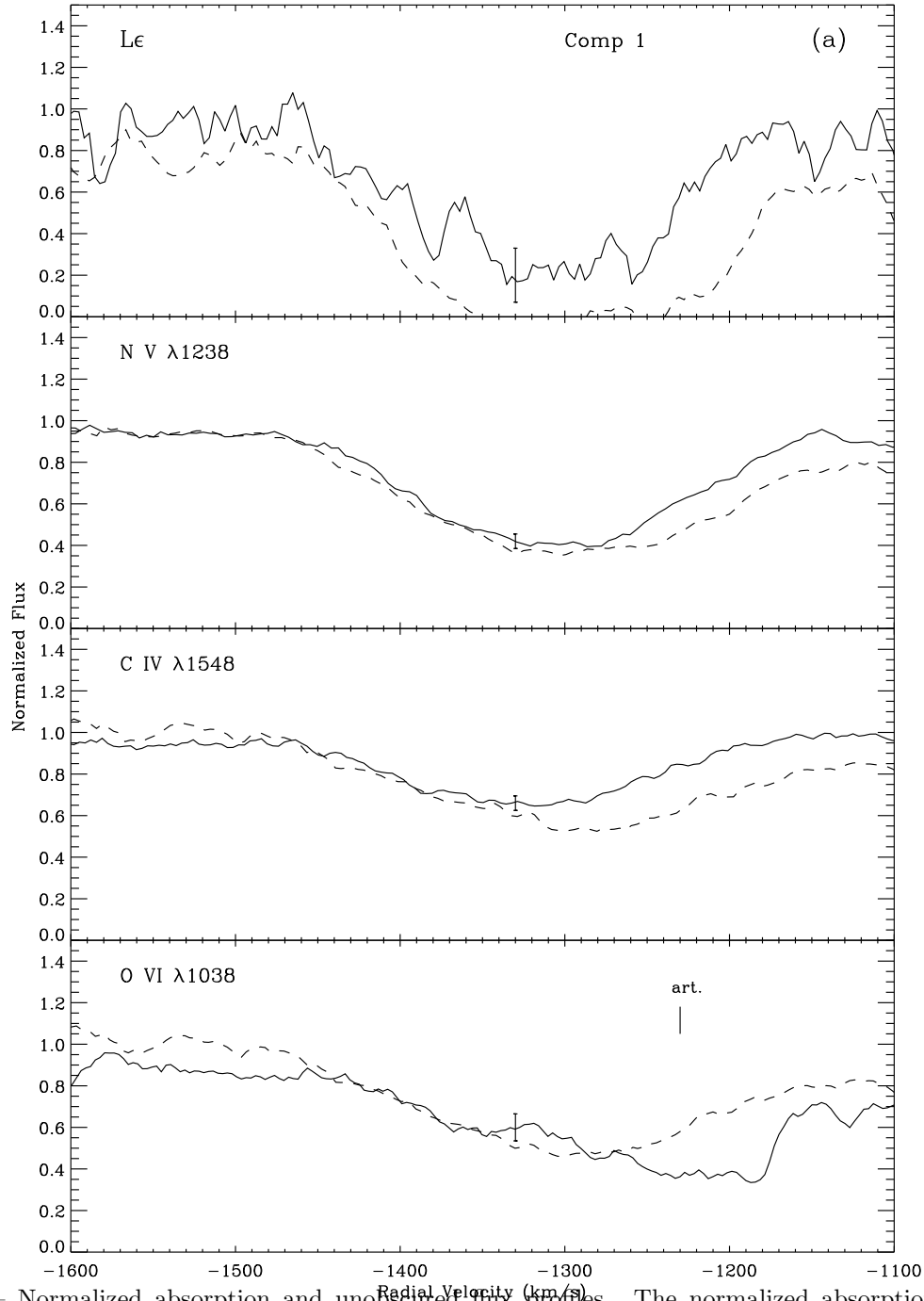


Fig. 5.— Normalized absorption and unobscured flux profiles. The normalized absorption profiles for component 1 (5a) and components 2 and 3 (5b) are plotted as solid lines. The unobscured normalized flux levels, $1 - C_f$, were computed using our C_f^c and C_f^l profiles derived for H I and are plotted as dashed lines. Typical error bars are marked on each spectrum with a vertical line. Galactic absorption has been divided out of each spectrum. The apparent absorption in the red wing of O VI component 1 at $v_r \sim -1200 \text{ km s}^{-1}$ is a detector artifact.

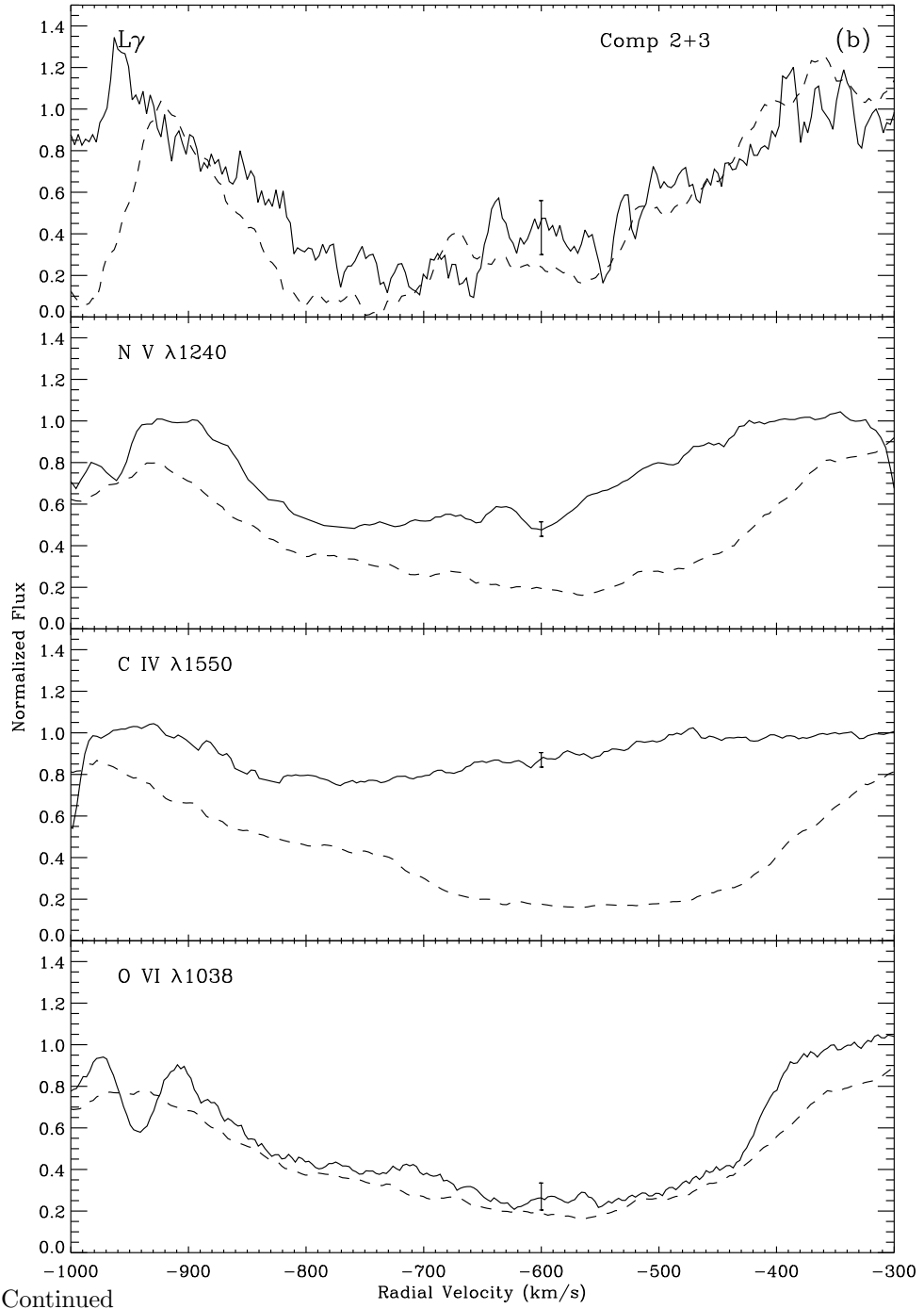


Fig. 5.— Continued